(article starts on next page)

The effect of cation substitution on the local coordination of protons in $Ba_2In_{1.85}M_{0.15}O_6H_2$ (M = In, Ga, Sc and Y)

Laura Mazzei [a], Fabio Piccinelli [b], Marco Bettinelli [b], Stewart F. Parker [c], Maths Karlsson [a,*]

[a] Department of Chemistry and Chemical Engineering, Chalmers University of Technology, SE-412 96 Göteborg, Sweden
[b] Luminescent Materials Laboratory, DB, Università di Verona, and INSTM, UdR Verona, Strada Le Grazie 15, 37134 Verona, Italy
[c] ISIS Facility, STFC Rutherford Appleton Laboratory, Chilton, Didcot, Oxon OX11 0QX, UK

ARTICLE INFO

ABSTRACT

We report on an investigation of the local structure and vibrational dynamics in the brownmillerite-based proton conductors $Ba_2In_{1.85}M_{0.15}O_6H_2$ with M = In, Ga, Sc and Y. The aim is to determine the effect of the cation (M) substitution on the local coordination environment of the protons. The techniques used are infrared spectroscopy and inelastic neutron scattering. The materials are characterized by two main types of proton sites, denoted as H(1) and H(2), which are featured by different local structures. We establish that the relative population of these two proton sites varies as a function of M. Specifically, it is found that, with respect to $Ba_2In_2O_6H_2$, the relative population of H(1) protons increases upon the substitution of In with any of the three different cations. The strongest effect is observed for M = Ga and Sc, whereas the effect observed for M = Y is minor. This new insight motivates efforts to unravel the mobility of the two types of protons, since then cation modification would offer a rational route for improving the proton conductivity of these types of materials.

1. Introduction

Brownmillerite-type oxides, of the general formula $A_2B_2O_5$, where A and B denote different metal ions, constitute an important class of proton and oxide-ion conducting materials, which makes them attractive for use in different technological applications [1–5]. Of specific concern in this work is $Ba_2In_2O_5$, which is characterized by an intergrowth of alternating (perovskite-like) InO_6 octahedral layers and InO_4 tetrahedral layers [6–8]. Upon exposure to humid conditions at elevated temperature, $Ba_2In_2O_5$ transforms into the hydrated phase $Ba_2In_2O_{5+x/2}H_x$ ($0 \leq x \leq 2$), where the protons are covalently bonded to oxygen atoms forming hydroxyl (OH^-) groups. The fully hydrated phase, $Ba_2In_2O_6H_2$, can be described as a "pseudo-cubic" structure, with the InO_4 tetrahedral layers of the dry phase transformed into heavily distorted octahedral layers, leading to a structure characterized by an alternation of distinct InO_6 octahedra layers (Fig. 1) [9–11].

As for the position of protons, $Ba_2In_2O_6H_2$ exhibits two main types of proton sites, labelled as H(1) and H(2). The H(1) protons are covalently bonded to the (apical) oxygen atoms that connect the alternating layers of undistorted and distorted InO_6 octahedra and form intra-octahedral hydrogen bonds to neighboring oxygen atoms. In comparison, the H(2) protons form covalent bonds to oxygen atoms in the heavily distorted octahedral layers and inter-octahedral hydrogen bonds to the oxygen

atoms of the same heavily distorted octahedral layers [9–14]. As in other proton conducting oxides, proton conduction in $Ba_2In_2O_6H_2$ occurs through a Grotthuss type mechanism separated into proton transfer between neighboring oxygen atoms and rotational motion of the covalent O—H bond between such transfers [2,15].

Recently, we performed a combined experimental and theoretical study of $Ba_2In_2O_6H_2$, based on infrared (IR) spectroscopy, inelastic neutron scattering (INS) and *ab initio* molecular dynamics simulations [14], showing that the different local coordination environments of the H(1) and H(2) proton lead to significantly different signatures in the vibrational spectra. Specifically, the vibrational dynamics of H(1) protons are manifested as δ[O—H(1)] and ν[O—H(1)] (bending and stretching) bands in the energy range of 80–120 meV and 400–450 meV, respectively. For the H(2) protons the corresponding δ[O—H(2)] and ν[O—H(2)] bands are instead located in the energy range of 120–160 meV and 200–400 meV [14]. The higher (lower) energy of the bending (stretching) band, with respect to those of the H(1) protons, is a result of stronger hydrogen bonding interactions of the H(2) protons. We further established that the amount of H(1) and H(2) protons is virtually the same in the fully hydrated phase, indicating full occupancy of the available H(2) sites and half occupancy of the H(1) sites.

In the present work, we investigate the effect of cation substitution on the local structure and vibrational dynamics of $Ba_2In_2O_6H_2$,

---
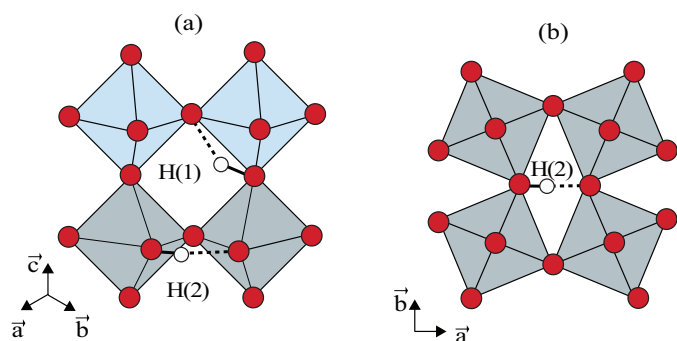
Fig. 1. (a) Sketch of the "pseudo-cubic" structure of $Ba_2In_2O_6H_2$ and (b) 2D top-view of the distorted octahedral layer containing the H(2)-type proton sites. Protons and oxygen atoms are marked by white and red spheres, respectively, whereas InO_6 octahedra of the undistorted and distorted layers are marked in light blue and grey color, respectively. The barium atoms have been omitted in the structures. Covalent and hydrogen bonds are distinguished by full and dashed black lines, respectively. (For interpretation of the references to color in this figure legend, the reader is referred to the web version of this article.)

specifically in the cation substituted materials $Ba_2In_{2-x}M_xO_6H_2$ with M = Ga, Sc, and Y. The techniques used are infrared spectroscopy and inelastic neutron scattering. Besides being of fundamental interest for increasing our understanding for the effect of cation substitution on the material's structural and dynamical properties, the cation substitution to $Ba_2In_2O_6H_2$ has been shown to lead to increased proton conductivity [4], which is of relevance for technological applications relying on fast proton conduction.

2. Experimental

2.1. Sample preparation

Powder samples of $Ba_2In_{1.85}M_{0.15}O_5$ (M = In, Ga, Sc, and Y) were prepared by solid state sintering by mixing stoichiometric amounts of the starting reactants ($BaCO_3$, In_2O_3, and M_2O_3). The sintering process was divided into three heat treatments, the first at 900 °C for 16 h and the others at 1300 °C for 24 h, with intermediate cooling, grinding and compacting of pellets between each heat treatment.

Analysis of powder X-ray diffraction (PXRD) patterns revealed that all samples are monophasic and characterized by an orthorhombic structure. PXRD data and analysis are provided as Supplementary Material.

Hydrated, proton conducting, samples were prepared by annealing the as-sintered powders at $\approx$ 300 °C under a flow of $N_2(g)$ saturated with water vapor for a period of a few days. This led to samples of the form $Ba_2In_{1.85}M_{0.15}O_6H_2$; here labelled as BIO ($M$ = In), 15Ga/BIO (M = Ga), 15Sc/BIO (M = Sc), and 15Y/BIO (M = Y).

2.2. Thermogravimetric analysis

Thermogravimetric (TG) measurements were performed on the nominally hydrated samples using a F1 Iris spectrometer from Netzsch. Each sample was heated in a flow of $N_2(g)$ (25 mL/min) from T = 25 °C to T = 800 °C at a heating rate of 5 °C/min.

2.3. Infrared spectroscopy

IR spectroscopy measurements were performed in the energy range 150–600 meV in diffuse reflectance mode using a Bruker IFS 66v/s FT-IR spectrometer equipped with a MCT detector and a KBr beam splitter. A measurement of a wrinkled Al-foil was used as a reference spectrum in the data treatment. Absorbance-like spectra of the samples were derived by taking the logarithm of the ratio between the reference spectrum and

the sample spectra.

2.4. Inelastic neutron scattering

The INS measurements were performed on MAPS [16] and TOSCA [17] at the ISIS Neutron and Muon Source at the Rutherford Appleton Laboratory (U.K.). For the present work, the key difference between the spectrometers is that at MAPS the momentum (Q, Å^{-1}) and energy ($\hbar\omega$, meV) transfer are measured independently, whereas TOSCA follows a fixed trajectory in (Q, $\hbar\omega$) space. Measurements on MAPS were performed at T = 10 K with an incident energy of 650 meV and using a Fermi chopper at 600 Hz. The samples, approximately 13 g of each composition, were loaded into aluminum sachets and the sachets into indium wire sealed thin-walled aluminum cans. Measurements on TOSCA were performed on the same samples at T < 10 K.
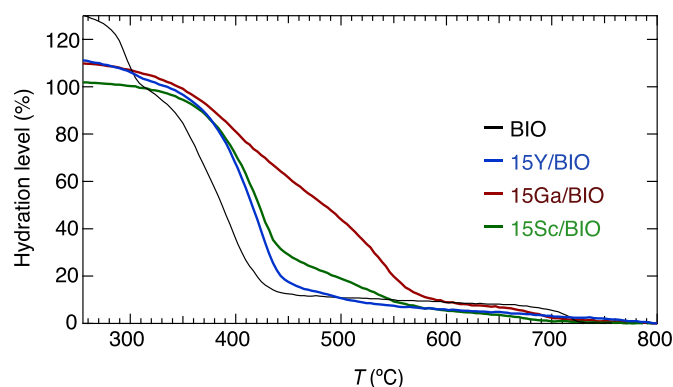
3. Results

3.1. Thermogravimetric analysis

Fig. 2 shows the hydration level of the nominally hydrated BIO, 15Y/BIO, 15Ga/BIO and 15Sc/BIO samples, as calculated from TG measurements by considering the samples to be completely dehydrated at T = 800 °C. The results confirmed that all samples were fully hydrated. The fact that the calculated hydration level is higher than 100%, especially for BIO, is likely related to the presence of a small amount of adsorbed surface water, which desorbs quickly upon heating.

We note that for the doped samples the curves are shifted towards higher temperature with respect to the undoped $Ba_2In_2O_5$ material, with the 15Ga/BIO sample exhibiting the highest dehydration temperature. One can also observe the presence of different regimes in the curves, which has been previously shown to relate to the formation of an intermediate phase upon dehydration, characterized by the presence of a fraction of thermally stable proton sites [12,14]. In particular, there are two possible types of proton configurations in the material, *type-1* and *type-2*. The difference in the configurations is in whether the H(1) protons form hydrogen bonds towards the undistorted tetrahedral layer or towards the highly distorted tetrahedral layer, and it has been shown that the *type-1* configuration is thermally more stable with respect to *type-2* [12]. Further, the same work has highlighted a preferential desorption of H(2) protons [12,14].

In this respect, the curves in Fig. 2 suggest a larger amount of thermally stable proton sites in the 15Ga/BZO sample. This could indicate a somehow larger amount of protons in the more stable *type-1* configuration. Another explanation could be that the Ga increases the thermal stability of the *type-2* configurations, or of the H(2) protons. Whichever the case, this different behavior might be related to the fact that Ga^{3+} can adopt both tetrahedral and octahedral coordination geometries,

Fig. 2. Hydration level of the nominally hydrated BIO, 15Y/BIO, 15Ga/BIO and 15Sc/BIO samples as calculated from the TG data.

whereas both Sc^{3+} and Y^{3+} can only adopt octahedral coordination geometries.

3.2. Infrared absorbance spectra

Fig. 3 shows the IR spectra for the four materials, BIO, 15Y/BIO, 15Ga/BIO and 15Sc/BIO, over the energy region 150–600 meV. In a qualitative analysis, all the spectra exhibit similar main bands, located at approximately 177, 250 (α_1), 290 (α_2), 355 (β), 420 (γ), and 530 meV. We remark that while the 15Y/BIO spectrum strongly resembles that of BIO, the 15Sc/BIO and 15Ga/BIO spectra are different because of a generally lower intensity of the α_1, α_2 and β bands.

On the basis of previous studies of the vibrational spectra of Ba$_2$In$_2$O$_6$H$_2$, the bands between 250 meV and 450 meV can be assigned to ν[O—H] modes in different local coordination environments [9,14], the 530 meV band to a combination of δ[O—H] and ν[O—H] vibrations [9,14], and the sharp 177 meV band to the vibrational mode of a carbonated impurity [14]. In more detail, γ is assigned to ν[O—H(1)] modes, whereas α_1, α_2, and β are assigned to ν[O—H(2)] modes [14]. The difference in vibrational energy between modes of the same type is a consequence of the varying degree of hydrogen bonding interactions in different local structures. One should note here that the IR absorbance cross section is not simply proportional to the number of vibrating species and may vary significantly with the degree of hydrogen bonding [18]. This explains why the α_1 and α_2 bands are quite strong in the spectrum, despite the fact that they are associated with a relatively small fraction ($\approx$10%) of H(2) protons having this vibrational frequency [14,18].

For a quantitative analysis of the spectra, we have performed a peak fitting analysis of the spectral region between 200 meV and 450 meV, for all the materials. Each spectrum can be adequately fit by a function consisting of seven Gaussian components and a linearly sloping background. Fig. 4(a) shows, as an example, the peak fitted spectrum of BIO. The peak fits of the other materials are shown in Fig. S3. The fitting parameters for all fits are compiled in Table 1.

While the use of more than seven Gaussian bands did not improve the quality of the fit, we found that the peak positions and widths were strongly correlated with each other. Thus, in order to obtain a reliable picture regarding the evolution of the different spectral contributions among the different materials, it was necessary to fix the positions of some Gaussians. Further information about this is given in Table 1.

As can be seen, the α_1, α_2, and β bands, which are assigned to ν[O—H
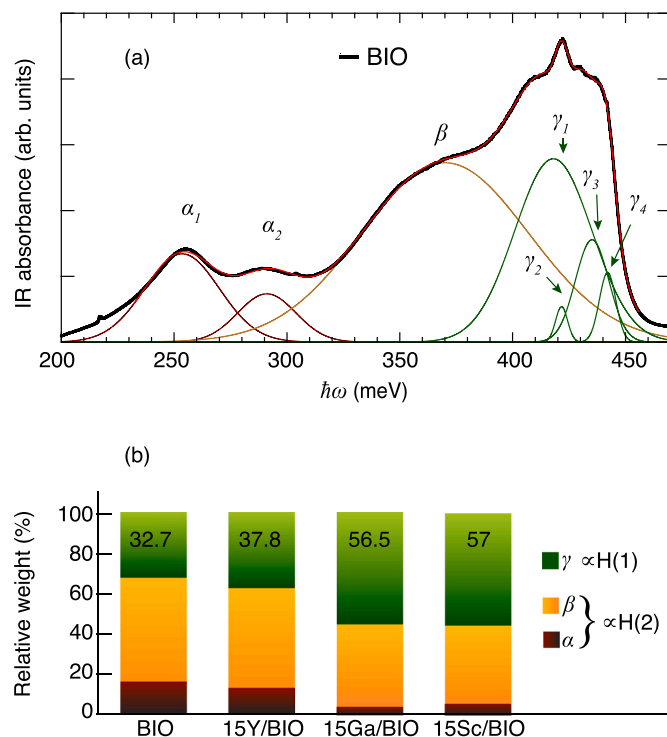
Fig. 4. (a) Peak fit of the IR spectrum of BIO, after background subtraction, and (b) relative weight of the spectral components of all the IR spectra (see text).

(2)] modes, are reproduced by three Gaussian bands, respectively, whereas the γ band, which is assigned to ν[O—H(1)] modes, is divided into four components (γ_1, γ_2, γ_3, γ_4). Interestingly, the relative weight of the H(2) related bands ($\alpha + \beta$) with respect to the H(1) band (γ), and thus the fraction of H(2) protons of all protons, is smaller for 15Y/BIO, and much smaller for 15Ga/BIO and 15Sc/BIO, compared to BIO [Fig. 4(b)].

3.3. Inelastic neutron scattering spectra

Fig. 5(a-b) show the INS spectra over the energy range 10–500 meV, as measured on MAPS and TOSCA, respectively. As for the IR spectra (Fig. 2), the INS spectra of the four materials are similar to each other. Both the MAPS and TOSCA spectra exhibit a strong and broad band at around 100 meV, which is assigned to δ[O—H] vibrations, and a weaker band at around 200 meV, which is assigned to second-order transitions [14]. At higher energies, the MAPS spectra exhibit a strong band around 400 meV, which is assigned to ν[O—H] vibrations [14]. Because TOSCA provides low sensitivity in this energy range, the ν[O—H] band cannot be observed in the TOSCA spectra. The bands below 50 meV are assigned to "riding modes", which refer to motions that involve the hydroxide group's oxygen atoms and for which the mode intensity is amplified due to the concurrent displacements of hydrogen atoms attached to the vibrating oxygen atoms [14]. However, the MAPS data below 50 meV are obscured by the elastic line and, therefore, these bands are not seen.

Fig. 4(c) shows a $S(Q, \hbar\omega)$ map of BIO, as obtained from the MAPS experiment. The maximum of the INS signal of the ν[O—H] mode occurs at larger Q values with respect to the δ[O—H] mode, as expected following a theoretical description of the INS intensity [18]. The $S(Q, \hbar\omega)$ maps for the doped materials, which are similar to the one in Fig. 4 (c), are shown in Fig. S4.

To capture the small, yet significant, differences between the spectra of the four different materials and as measured on two instruments, we performed a peak fitting analysis of each spectrum over the range of 40–350 meV. We find that the TOSCA spectra can be adequately reproduced by a function consisting of nine Gaussian bands and a
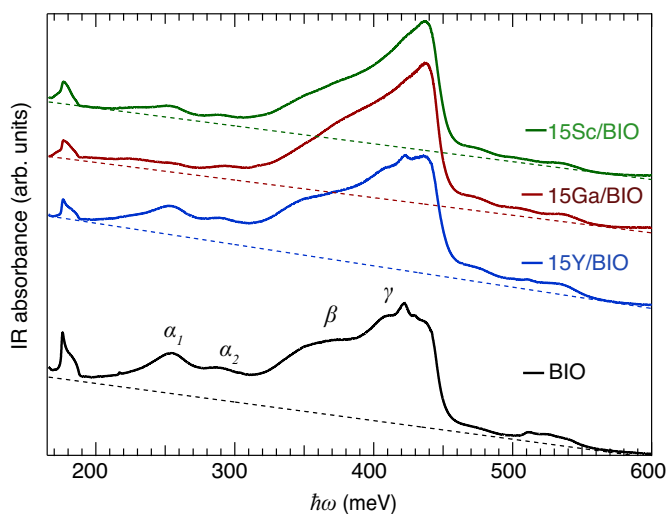

Fig. 3. IR absorbance spectra of BIO, 15Y/BIO, 15Ga/BIO and 15Sc/BIO. The spectra are vertically offset for clarity. Dashed lines represent the linear backgrounds as fitted to the IR spectra.

Table 1

Fitting parameters extracted from the analysis of the IR and INS spectra of all samples. $\hbar\omega$ represents the peak position (in meV) of each Gaussian band, and the relative weight is calculated from the integrated intensity. Values marked with an asterisk were fixed in the fitting, and the P_1 and P_2 peaks were fixed to have the same FWHM. Values within parentheses are standard errors on the last digits.

Label	$\hbar\omega$ (meV)				Relative weight (%)			
	BIO	15Y/BIO	15Ga/BIO	15Sc/BIO	BIO	15Y/BIO	15Ga/BIO	15Sc/BIO
IR								
α_1	253.5*	253.5*	253.5*	253.5*	11.24(4)	9.77(3)	3.30(1)	4.29(3)
α_2	291*	291*	291*	291*	4.79(3)	3.00(2)	2.20(2)	1.64(2)
β	370*	370*	370*	370*	51.2(2)	49.36(5)	38.0(1)	37.35(5)
γ					32.7(4)	37.8(2)	56.5(8)	57(2)
γ_1	418*	418*	418*	418*	24.2(2)	26.28(4)	41.8(1)	37.1(1)
γ_2	421.68(2)	421.52(5)	426.4(6)	424(1)	0.72(1)	0.75(2)	5.7(3)	7.1(6)
γ_3	435.1(1)	437.46(6)	434.80(6)	434.6(1)	5.8(1)	9.64(7)	3.8(3)	6.5(7)
γ_4	442*	442*	442*	442*	1.958(5)	1.21(3)	5.08(7)	6.0(2)
INS - TOSCA.								
P_1	64(2)	62(7)	62.8(6)	62.4(6)	7.6 (1)	11(3)	11.43(4)	11.58(4)
P_2	83(4)	77(20)	77(2)	76(2)	15.7(6)	10(16)	13.2(1)	10.8(1)
B_1	96(2)	90(70)	91(2)	91(1)	18.9(3)	20(80)	20.9(1)	24.3(1)
B_2	108(1)	104(70)	105(1)	106(1)	18.9*	20*	20.9*	24.3*
C_2	125(2)	123(23)	123(3)	125(3)	19.39(8)	19(96)	16.7(2)	14.5(2)
C_2	148(1)	150(22)	145(3)	148(3)	19.39*	19*	16.7*	14.5*
INS - MAPS.								
P_1	71(3)	70(7)	66(3)	65(2)	7.5(3)	11(3)	8.4(8)	5(1)
P_2	85(7)	85(16)	78(6)	76(5)	13(2)	19(26)	8(3)	3(1)
B_1	98(5)	100(30)	90(9)	90(3)	23.6(6)	23(12)	27(2)	37(2)
B_2	111(3)	110(13)	107(4)	112(2)	23.6*	23*	27*	37*
C_1	128(5)	130(12)	126(8)	134(3)	15.9(4)	12(3)	14.4(9)	8.6(5)
C_2	148(2)	149(9)	146(5)	153(3)	15.9*	12*	14.4*	8.6*

baseline of the form $a\log(b\hbar\omega)$, where a and b are constants. The same fitting procedure was applied to the fitting of the MAPS spectra, but with a baseline of the form $Ae^{-(x/\tau)}$, where A and τ are constants. Fig. 6 shows, as an example, the peak fit to the BIO spectra as measured on the two instruments. The peak fitting analysis of the other materials are shown in Fig. S5, and the fit parameters for all fits are shown in Table 1.

In agreement with previous investigations of BIO [14], the 50–170 meV range of the INS spectrum can be divided into six components, here labelled as P_1, P_2, B_1, B_2, C_1 and C_2. The B_1 and B_2 components are assigned to the "in-plane" and "out-of-plane" $\delta[O—H(1)]$ vibrational modes, whereas the C_1 and C_2 components are assigned to the "in-plane" and "out-of-plane" $\delta[O—H(2)]$ vibrational modes. The P_1 and P_2 components are assigned to vibrational modes of the brownmillerite lattice. In addition to these six bands, three additional Gaussians, at approximately 190 meV, 250 meV and 290 meV were fit to the spectra. These bands account for vibrational intensity associated with higher-order transitions, but, since the position and intensity of these peaks are not relevant to this analysis, they are not further discussed in the remainder of this work.

One should note that the B_1 and B_2 components relate to two different motions of the same species, *i.e.* the H(1) protons, and, since the INS intensity for a given vibrational mode ω_i is directly proportional to the number of vibrating species, the intensity of these bands (B_1 and B_2) are correlated to each other. In a simplified description [19,20],

$$S(Q, \hbar\omega_i) \propto N \cdot \left(Q^2 u_i^2\right) e^{-Q^2 u_{tot}^2/3} \tag{1}$$

where N is the number of vibrating species and u_{tot}^2 is the total mean square displacement of the atoms. u_i is the amplitude of the vibration, with $u_i^2 \propto 1/\omega_i$ for harmonic vibrations. We remark that in the case of TOSCA the INS spectra are collected on fixed $\omega - Q$ trajectories, such that $Q^2 \propto \hbar\omega$, whereas on MAPS the INS spectra are obtained by integrating over a large Q-interval.

In order to include the correlation between the intensity of the B_1 and B_2 bands in the fit, we have made the approximation that the difference in intensity between the two $\delta[O—H(1)]$ bands is small, within the error of the fit. This approximation reflects the fact that the two modes are close in energy ($\hbar\omega_{B1} \approx \hbar\omega_{B2}$), thus characterized by similar amplitude ($u_{B1} \approx u_{B2}$). Therefore we have constrained the integrated intensity of

the two bands to have same values. The same constraint was applied to C_1 and C_2.

Analogously, one may argue that the peak positions should be fixed to the same values in the fitting of the TOSCA and MAPS spectra of a given material. However, in order to allow for some differences due to the differently probed Q values, these were not fixed in the fitting procedure. Nevertheless, the peak positions obtained from the two different fits are in good agreement to each other, making the results more reliable since no agreement among the fit parameters was imposed *a priori*.

Since the INS intensity is proportional to the amount of vibrating species, the relative weight of the B and C components reflects the relative amount of H(1) and H(2) type protons in the materials. Using this relationship, Fig. 6(c-d) shows the relative amount of H(1) and H(2) protons, as derived from the peak fitting parameters from the two different instruments (Table 1). For the TOSCA data [Fig. 6(c)], we observe that the relative amount of H(1) and H(2) protons are roughly the same for the BIO sample, in agreement with our previous study [14], whereas for the doped materials the relative amount of H(1) protons increases, especially for 15Ga/BIO and 15Sc/BIO.

For the MAPS data [Fig. 6(d)], we observe a similar dependency. However, a major difference with respect to the TOSCA data is that for the BIO sample the relative amount of H(1) is higher than the relative amount of H(2). Additionally, in the MAPS data there is almost no variation between the values for 15Y/BIO and 15Sc/BIO. In this respect, we remark that the values obtained from the fits of 15Y/BIO are characterized by a larger uncertainty with respect to the other materials (Table 1). At the same time, we note (see Table 1) that the relative contribution of the lattice modes (P) varies between MAPS and TOSCA data, which may indicate a redistribution of weight, during the fit, between the P and B components. Despite these variations between the TOSCA and MAPS data, we observe a unifying, clear trend of an increasing amount of H(1) protons with respect to the H(2) protons, upon doping, with the effect being largest for 15Sc/BIO and smallest for 15Y/BIO. Notably, the same trend is observed in the corresponding IR spectra.
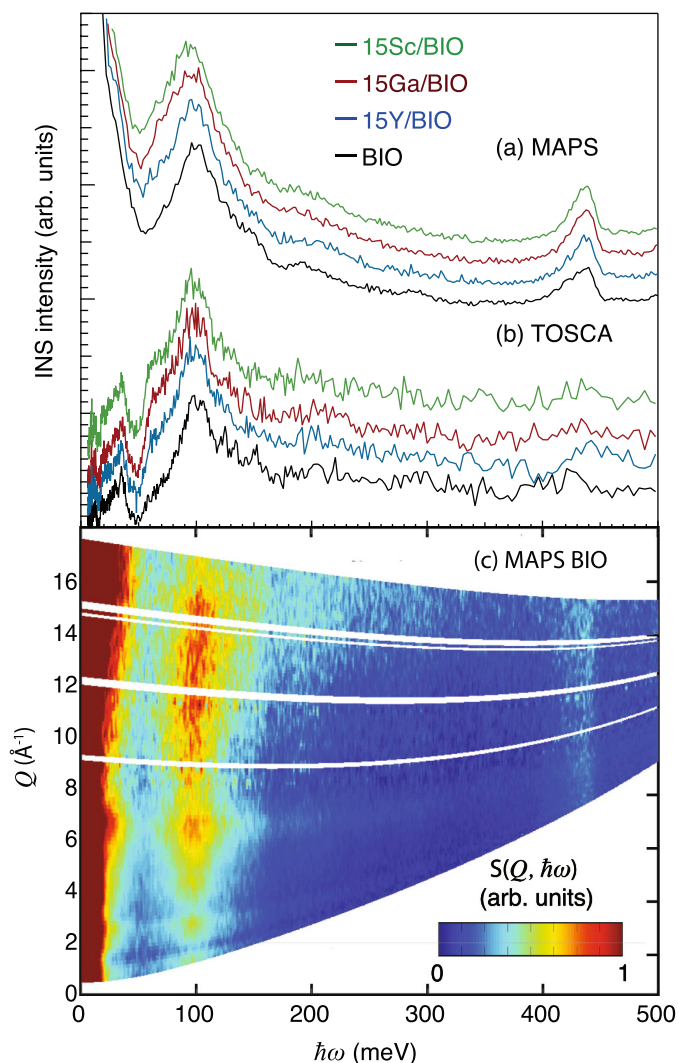
Fig. 5. INS spectra at $T < 10$ K of BIO, 15Y/BIO, 15Ga/BIO and 15Sc/BIO as recorded on (a) MAPS and (b) TOSCA. Spectra are vertically offset for clarity. (c) INS intensity $S(Q, \hbar\omega)$ of BIO as measured on MAPS.

4. Discussion

A key observation of the present IR and INS investigations of BIO, 15Y/BIO, 15Ga/BIO and 15Sc/BIO regards the occupancies of the two main types of proton sites, H(1) an H(2), which evolve from largely the same for BIO and 15Y/BIO, to a significantly increased (decreased) weight of the H(1) (H(2)) proton site for 15Ga/BIO and 15Sc/BIO. We notice that all the materials are characterized by the same pseudo-cubic layered structure, hence one can expect the available number of H(1) and H(2) proton sites to be unaltered upon doping. In light of this, our results point to the fact that with doping the H(1) proton sites become more energetically favorable, hence more populated, at the expenses of the H(2) proton sites.

A priori, one may have expected that the relative weight of the H(1) to H(2) protons shows some simple dependence upon the ionic radii of the respective dopant atom. However, this is not the case, as 15Ga/BIO, the material with the smallest dopant atom (Ga, 62 pm), shows a relative weight of H(1) to H(2) protons that is approximately intermediate to one of the other materials (*cf.* Fig. 4(b) and Fig. 6(c-d)).

In this context, we remark that, according to previous studies, the effect of cation substitution on the structure of the respective dehydrated compounds depends on the dopant species. For instance, Y-doped Ba$_2$In$_2$O$_5$ was found to be isostructural to Ba$_2$In$_2$O$_5$, *i.e.* orthorhombic,
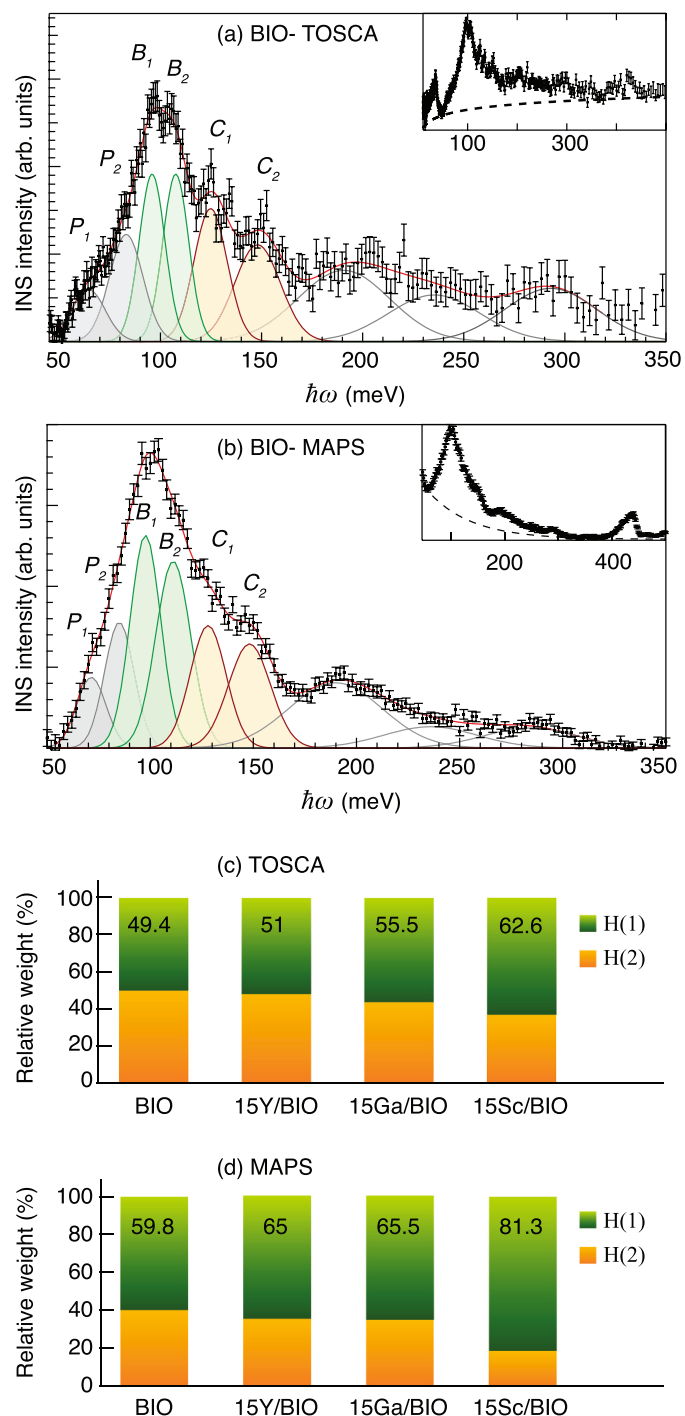
Fig. 6. Peak fit of the (a) TOSCA and (b) MAPS spectra, after baseline correction. The INS spectra before correction and the baselines fitted to the spectra (see text) are shown in insets. (c-d) Relative population of H (1) and H (2) proton sites as obtained from the TOSCA (c) and MAPS (d) INS spectra (see text).

only for $x < 0.2$ [4,21], whereas Ga- and Sc-doped Ba$_2$In$_2$O$_5$ were reported to be orthorhombic up to $x = 0.4$ and $x = 0.5$, respectively [4,21–23]. We note that also in this case there is no clear dependence on the ionic radii. As another example, it has been shown that the order-disorder transition temperature of oxygen vacancies in cation substituted Ba$_2$In$_2$O$_5$ depends on the relative size of the dopant with respect to In [24]. Furthermore, we note that while Sc^{3+} prefers octahedral configurations, Ga^{3+} can adopt both tetrahedral and octahedral coordination geometries. Indeed, in a recent investigation of

$Ba_2In_{2-x}Ga_xO_5$ with $x > 0.2$, it was shown that the Ga^{3+} ions are preferentially tetrahedrally coordinated [22,23]. These results point towards a complex relationship between the nature of proton sites, local structural distortions, and cation substitution.

In light of the finding of that the relative occupation of H(1) and H(2) protons can be changed as an effect of cation substitution, it would be interesting to know how this affects the materials' proton transport properties. Of relevance here, Noirault et al. [4], investigated the proton conductivity of Sc and Y substituted $Ba_2In_2O_5$ and established that cation substitution leads to an increase of the total (bulk + grain boundary) conductivity. According to their results, $Ba_2In_{1.85}M_{0.15}O_6H_2$ with $M = $ Sc and Y exhibit a similar activation energy for the total proton conductivity [4], but, note, that does not provide any direct information on the local mobility of the H(1) and H(2) protons in the material.

More recently, Perrichon et al. [14] showed that the H(2) protons are characterized by the strongest hydrogen bond, hence their mobility is most probably limited by a relatively high energy barrier for the O—H rotational motion, whereas for the H(1) protons, is was shown that they tend to order (pair), which works as an additional energy barrier. Because of these differences, it can be expected that the H(1) and H(2) protons are characterized by different proton mobilities, or, in other words, that one species is more mobile than the other. Further, it has been suggested that the full occupancy of the H(2) proton sites might hinder the diffusion of protons in the highly distorted layer. [9]. All this raises the natural question of whether there is a relative level of occupancy which maximizes the proton diffusion. However, details on the local mobility of these two different types of proton sites remain to be clarified. In view of the fact that various cation substitutions can be used as a means to shift the relative occupation of the two proton sites, the unraveling of the atomic-scale proton mobility in $Ba_2In_{1.85}M_{0.15}O_6H_2$ with $M = $ Ga, Sc and Y, would offer a rational route for improving the bulk proton conductivity in brownmillerite-type proton conducting oxides.

5. Conclusions

We have investigated the effect of cation substitution on the local coordination environment and vibrational dynamics of protons in the brownmillerite-based proton conducting material $Ba_2In_2O_6H_2$, with a focus on $Ba_2In_{1.85}M_{0.15}O_6H_2$ with $M = $ Ga, Sc, and Y, using IR spectroscopy and INS. In agreement with previous studies on $Ba_2In_2O_6H_2$, all materials are found to exhibit two main types of proton locations, denoted as H(1) and H(2), which are characterized by different local structural surroundings in the material. The main effect of the cation substitution on the proton coordination environment is an increased population of H(1) protons and a decreased population of H(2) protons, with the effect being largest for Ga and Sc as substituting cations.

The evidence that the relative population of the different proton sites can be tuned upon cation substitution points towards the possibility for rational tuning of the materials' proton conducting properties should the local mobilities of H(1) and H(2) protons be elucidated. Therefore, our new insight into the local structure and dynamics of $Ba_2In_{1.85}M_{0.15}O_6H_2$ with $M = $ Ga, Sc, and Y, motivates efforts to unravel the atomic-scale proton mobilities in these materials, by, *e.g.*, quasi-elastic neutron scattering techniques [25], as a route towards the design of materials with improved proton conductivity.

Author statement

The authors declare that all authors have contributed significantly to the preparation of this manuscript. Specifically, M. K. performed the INS experiments, assisted by S. F. P., whereas M. K. and L. M. interpreted the INS data. The samples were prepared by F. P. and M. B., who also analyzed in detail their structural properties with the use of XRD. The paper was mostly written by L. M. and M. K., but all authors provided critical comments on the work and to the writing of the paper. M. K. designed the study.

Declaration of Competing Interest

The authors declare that they have no known competing financial interests or personal relationships that could have appeared to influence the work reported in this paper.

Appendix A. Supplementary data

Supplementary material includes PXRD data and analysis for all samples (Fig. S1); peak fitted IR absorbance spectra for 15Y/BIO, 15Ga/BIO and 15Sc/BIO (Fig. S2); INS maps and peak fitted INS spectra for 15Y/BIO, 15Ga/BIO and 15Sc/BIO (Fig. S3-S4).

References

[1] G.B. Zhang, D.M. Smyth, Defects and transport of the brownmillerite oxides with high oxygen ion conductivity–$Ba_2In_2O_5$, Solid State Ionics 82 (3–4) (Dec 1995) 161–172.

[2] G.B. Zhang, D.M. Smyth, Protonic conduction in $Ba_2In_2O_5$, Solid State Ionics 82 (3–4) (Dec 1995) 153–160.

[3] Neelima Mahato, Amitava Banerjee, Alka Gupta, Shobit Omar, Kantesh Balani, Progress in material selection for solid oxide fuel cell technology: a review, Prog. Mater. Sci. 72 (Jul 2015) 141–337.

[4] Samuel Noirault, Eric Quarez, Yves Piffard, Olivier Joubert, Water incorporation into the $Ba_2(In_{1-x}M_x)_2O_5$ (M=Sc^{3+} $0 \le x < 0.5$ and M = Y^{3+} $0 \le x \le 0.35$) system and protonic conduction, Solid State Ionics 180 (20) (Aug 2009) 1157–1163.

[5] N. Tarasova, I. Animitsa, The influence of anionic heterovalent doping on transport properties and chemical stability of F-, Cl-doped brownmillerite $Ba_2In_2O_5$, J. Alloys Compd. 739 (Mar 2018) 353–359.

[6] V. Jayaraman, A. Magrez, M. Caldes, O. Joubert, F. Taulelle, J. Rodriguez-Carvajal, Y. Piffard, L. Brohan, Characterization of perovskite systems derived from $Ba_2In_2O_5$: part II: the proton compounds $Ba_2In_{2(1-x)}Ti_{2x}O_{4+2x}(OH)_y$ [$0 \le x \le 1$; $y \le 2(1 - x)$], Solid State Ionics 170 (1) (May 2004) 25–32.

[7] S.A. Speakman, J.W. Richardson, B.J. Mitchell, S.T. Misture, In-situ diffraction study of $Ba_2In_2O_5$, Solid State Ionics 149 (3) (Aug 2002) 247–259.

[8] P. Berastegui, S. Hull, F.J. García-García, S.-G. Eriksson, The crystal structures, microstructure and ionic conductivity of $Ba_2In_2O_5$ and $Ba(In_xZr_{1-x})O_{3-x/2}$, J. Solid State Chem. 164 (1) (Feb 2002) 119–130.

[9] Johan Bielecki, Stewart F. Parker, Dharshani Ekanayake, Seikh M.H. Rahman, Lars Börjesson, Maths Karlsson, Short-range structure of the brownmillerite-type oxide $Ba_2In_2O_5$ and its hydrated proton-conducting form BaInO3H, J. Mater. Chem. A 2 (40) (Sep 2014) 16915–16924.

[10] V. Jayaraman, A. Magrez, M. Caldes, O. Joubert, M. Ganne, Y. Piffard, L. Brohan, Characterization of perovskite systems derived from $Ba_2In_2O_5$: part I: the oxygen-deficient $Ba_2In_{2(1-x)}Ti_{2x}O_{5+x}\square_{1-x}$ ($0 \le x \le 1$) compounds, Solid State Ionics 170 (1–2) (May 2004) 17–24.

[11] Jean-Raphaël Martinez, Chris E. Mohn, Svein Stølen, Neil L. Allan, $Ba_2In_2O_4(OH)_2$: Proton sites, disorder and vibrational properties, J. Solid State Chem. 180 (12) (Dec 2007) 3388–3392.

[12] Johan Bielecki, Stewart F. Parker, Laura Mazzei, Lars Börjesson, Maths Karlsson, Structure and dehydration mechanism of the proton conducting oxide $Ba_2In_2O_5(H_2O)_x$, J. Mater. Chem. A 4 (Jan 2016) 1224–1232.

[13] R. Dervişoğlu, D.S. Middlemiss, F. Blanc, Y.-L. Lee, D. Morgan, C.P. Grey, Joint experimental and computational ^{17}O and ^{1}H solid state NMR study of $Ba_2In_2O_4(OH)_2$ structure and dynamics, Chem. Mater. 27 (11) (Jun 2015) 3861–3873.

[14] A. Perrichon, M. Jiménez-Ruiz, L. Mazzei, S.M.H. Rahman, M. Karlsson, Local structure and vibrational dynamics of proton conducting $Ba_2In_2O_5(H_2O)_x$, J. Mater. Chem. A 7 (29) (Jul 2019) 17626–17636.

[15] K.D. Kreuer, Aspects of the formation and mobility of protonic charge carriers and the stability of perovskite-type oxides, Solid State Ionics 125 (1–4) (Oct 1999) 285–302.

[16] Stewart F. Parker, D. Lennon, P.W. Albers, Vibrational spectroscopy with neutrons: a review of new directions, Appl. Spectrosc. 65 (12) (Dec 2011) 1325–1341.

[17] S.F. Parker, F. Fernandez-Alonso, A.J. Ramirez-Cuesta, J. Tomkinson, S. Rudic, R. S. Pinna, G. Gorini, J. Fernández Castañón, Recent and future developments on TOSCA at ISIS, J. Phys. Conf. Ser. 554 (1) (Nov 2014) 012003.

[18] Laura Mazzei, Adrien Perrichon, Alessandro Mancini, Göran Wahnström, Lorenzo Malavasi, Stewart F. Parker, Lars Börjesson, Maths Karlsson, Local structure and vibrational dynamics in indium-doped barium zirconate, J. Mater. Chem. A 7 (13) (Mar 2019) 7360–7372.

[19] P.C.H. Mitchell, S.F. Parker, A.J. Ramirez-Cuesta, J. Tomkinson, Vibrational Spectroscopy with Neutrons, Word Scientific, Singapore, 2005.

[20] J. Tomkinson, S.F. Parker, D. Lennon, No evidence for Evans' holes in the A, B, C vibrational structure of potassium dihydrogen arsenate, J. Chem. Phys. 133 (3) (Jul 2010) 034508.

[21] Takahisa Omata, Masao Kita, Yuji Goto, Takahiko Okura, Shinya Otsuka-Yao-Matsuo, Formation and thermal stability of hydrate-like compounds of $Ba_2(In_{1-x}M_x^{III})_2O_5 \cdot nH_2O$ (M^{III}=Ga, Sc, Lu, and Y), J. Electrochem. Soc. 152 (6) (Apr 2005) A1068.

[22] T. Yao, Y. Uchimoto, M. Kinuhata, T. Inagaki, H. Yoshida, Crystal structure of Ga-doped $Ba_2In_2O_5$ and its oxide ion conductivity, Solid State Ionics 132 (3) (Jul 2000) 189–198.

[23] Christophe Didier, John Claridge, Matthew Rosseinsky, Crystal structure of brownmillerite Ba_2InGaO_5, J. Solid State Chem. 218 (Oct 2014) 38–43.

[24] Tuan Q. Ta, Toshihide Tsuji, Yasuhisa Yamamura, Thermal and electrical properties of $Ba_2In_2O_5$ substituted for In-site by rare earth elements, J. Alloys Compd. 408–412 (Feb 2006) 253–256.

[25] M. Karlsson, Proton dynamics in oxides: insight into the mechanics of proton conduction from quasielastic neutron scattering, Phys. Chem. Chem. Phys. 17 (1) (Jan 2015) 26–38.